

Synergy of Cu(I) and oxygen vacancies in CO₂ hydrogenative coupling to ethanol on Cu/CeO_{2-x} catalysts

Joaquin Herrero^{1,§}, Peilei He^{2,§}, Fan Yang², Jiaping Weng¹, Nicole J. LiBretto³, Daniela S. Mainardi¹, Jeffrey T. Miller³, Yue Wu², and Yang Xiao¹

¹ Department of Chemical Engineering and Institute for Micromanufacturing, Louisiana Tech University, 505 Tech Drive, Ruston, LA 71272, USA

² Department of Chemical and Biological Engineering, Iowa State University, 618 Bissell Road, Ames, IA 50011, USA

³ Davidson School of Chemical Engineering, Purdue University, 480 Stadium Mall Drive, West Lafayette, IN 47907, USA

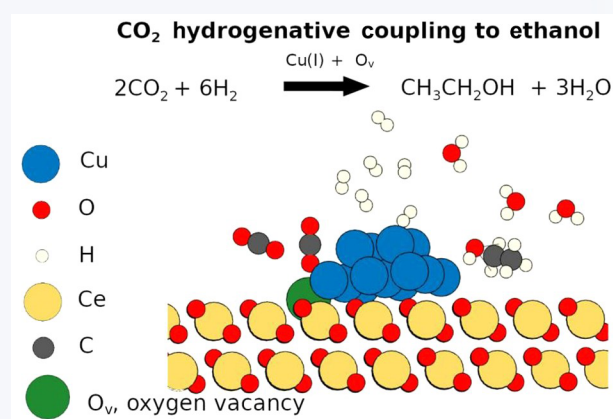
§ Joaquin Herrero and Peilei He contributed equally to this work.



Cite this article: Nano Research, 2025, 18, 94907518. <https://doi.org/10.26599/NR.2025.94907518>

ABSTRACT: Hydrogenative coupling of CO₂ to ethanol presents a sustainable pathway for carbon neutralization, yet the fundamental active sites and reaction pathway/mechanism remain unclear. Here, we investigate CO₂ hydrogenative coupling over Cu/CeO_{2-x} catalysts, achieving an optimal CO₂ conversion of ~ 5% and ethanol selectivity of ~ 95% under 30 atm, H₂/CO₂ = 3, at 240 °C, and gas hourly space velocity (GHSV) = 120 mL·g_{cat}⁻¹·h⁻¹. We revealed that both Cu(I) and oxygen vacancies (O_v) serve as active sites, with turnover frequencies (TOFs) of 0.23 h⁻¹ per O_v site and 3.97 h⁻¹ per Cu(I) site, respectively. We also concluded that neither Cu(I) nor O_v can function independently; both Cu(I) and O_v are required for CO₂ activation and ethanol formation. *Operando* Fourier-transform infrared (FTIR) spectroscopy and density functional theory (DFT) calculations identify CH₂OH* and CH₂* as key intermediates in the C–C coupling step. These findings establish a mechanistic framework for CO₂ hydrogenative coupling and provide valuable insights for designing more efficient catalysts for ethanol synthesis from CO₂ conversion.

KEYWORDS: CO₂ hydrogenation, CO₂ to ethanol, Cu/CeO₂ catalysts, oxygen vacancy, synergistic effect



1 Introduction

The conversion of CO₂ into value-added chemicals and fuels is a crucial challenge in sustainable energy and carbon neutralization strategies. Among various CO₂ hydrogenation products, ethanol is particularly attractive due to its potential as widely used fuel/fuel additive, hydrogen carrier, and chemical feedstock for industrial applications. As compared to methanol (CH₃OH), ethanol offers advantages, such as higher energy density, improved blending compatibility with gasoline, and lower volatility, making it a more suitable candidate for transportation fuels. However, hydrogenative

coupling of CO₂ to ethanol remains challenging due to competing reaction pathways that favor methanol, methane (CH₄), and CO formation, often resulting in poor ethanol selectivity. Understanding the reaction mechanism, particularly the active sites and intermediates responsible for C–C bond formation, is crucial for developing efficient catalysts [1–4].

Various catalyst systems have been explored for CO₂ hydrogenation to ethanol, including Cu-, Pd-, and Rh-based catalysts, bimetallic formulations, and oxide-supported systems, each offering distinct advantages and challenges [5, 6]. Cu-based catalysts have gained significant attention due to their low cost, tunable redox properties, and moderate binding strength for CO₂ activation, making them particularly suitable for selective CO₂ hydrogenation. However, the primary limitation of monometallic Cu catalysts is their tendency to favor methanol production rather than C–C coupling to ethanol. Pd- and Rh-based catalysts, on the other hand, exhibit higher activity and selectivity toward C₂

Received: February 26, 2025; Revised: April 25, 2025

Accepted: April 28, 2025

✉ Address correspondence to Yang Xiao, yxiao@latech.edu; Yue Wu, yuewu@iastate.edu; Jeffrey T. Miller, jeffrey-t-miller@purdue.edu

oxygenates due to their stronger CO₂ activation capabilities and ability to stabilize key reaction intermediates. Despite these advantages, Pd and Rh catalysts suffer from high costs, rapid deactivation, and methane formation, which hinder their large-scale application [7–9].

To address these limitations, bimetallic catalysts, such as Cu–Zn, Cu–Fe, and Pd–Cu systems, have been developed to improve selectivity and stability by tuning the electronic and geometric properties of the active metal sites [10–14]. Additionally, oxide-supported catalysts, particularly those utilizing the cerium(IV) oxide (CeO₂), TiO₂, and ZnO, play a crucial role in enhancing CO₂ adsorption, stabilizing intermediates, and modulating metal oxidation states. Among these, CeO₂-supported catalysts stand out due to their high oxygen storage capacity and ability to create oxygen vacancies (O_v), which facilitate CO₂ activation and hydrogenation. The strong metal–support interactions (MSI) in Cu/CeO₂ catalysts have been shown to stabilize Cu^I species, which are crucial for selective CO₂ hydrogenation to ethanol. Despite these advancements, the precise role of Cu^I and O_v in facilitating C–C bond formation remains poorly understood, necessitating further mechanistic investigations to guide rational catalyst design [15–18].

In this study, we investigate the hydrogenative coupling of CO₂ to ethanol over Cu/CeO_{2-x} catalysts, focusing on the synergy of Cu^I and O_v as active sites. *Quasi in situ* X-ray photoelectron spectroscopy (XPS), *operando* Fourier-transform infrared (FTIR) spectroscopy, and density functional theory (DFT) calculations were employed to identify the key intermediates involved in ethanol formation. We find that both Cu^I and O_v are essential for CO₂ activation and ethanol synthesis, with turnover frequencies (TOFs) of 0.23 h⁻¹ per O_v site and 3.97 h⁻¹ per Cu^I site. Notably, neither Cu^I nor O_v alone is sufficient, and their synergy is required for CO₂ conversion to ethanol. *Operando* FTIR and DFT calculations confirm that CH₂OH and CH₂ are the primary C–C coupling intermediates.

2 Experimental

2.1 Catalyst synthesis

Copper was loaded onto CeO₂ (> 99.9% trace metals basis, Sigma-Aldrich) support using the incipient-wetness impregnation (IWI) method. Copper(II) nitrate trihydrate (Cu(NO₃)₂·3H₂O, > 99.9% trace metals basis, Sigma-Aldrich) served as the copper precursor. In a typical synthesis, the required amount of Cu(NO₃)₂·3H₂O was dissolved in deionized (DI) water to prepare a solution containing 0.04 g_{Cu}·mL⁻¹. The Cu solution was then impregnated onto the CeO₂ support. After impregnation, the catalysts were dried overnight under vacuum at 65 °C. Prior to testing, the catalysts were reduced in a 10% H₂/He atmosphere at 400 °C for 2 h. These prepared catalysts were subsequently used for catalytic performance testing and kinetic measurements for CO₂ hydrogenative coupling to ethanol.

2.2 Catalyst characterization

The physicochemical properties of the Cu/CeO_{2-x} catalysts were assessed using multiple characterization techniques. Brunauer–Emmett–Teller (BET) surface area, pore size, and pore volume measurements were performed using N₂ adsorption–desorption at 77 K with a Micromeritics ASAP 2020 apparatus. Prior to analysis, the samples were degassed at 300 °C for 8 h.

Elemental analysis was conducted with a Thermo Fisher Scientific X Series 2 inductively coupled plasma-atomic emission spectrometer (ICP-AES) to determine the copper loading.

X-ray diffraction (XRD) patterns were recorded at room temperature on a Bruker diffractometer with a Cu K α radiation source ($\lambda = 1.5406 \text{ \AA}$) to analyze the crystallographic structure. Morphological and compositional analyses were performed using scanning electron microscopy (SEM) and high-resolution, high-angle annular dark-field (HAADF) scanning transmission electron microscopy (STEM) imaging. These measurements were carried out on a Titan Themis 300 probe-corrected TEM equipped with a Super-X EDX detector at the Sensitive Instrument Facility of Ames Laboratory. X-ray absorption spectroscopy (XAS) experiments were conducted at the 9-BM beamline of the Advanced Photon Source (APS), Argonne National Laboratory. Measurements were taken at the Cu K-edge (8.979 keV) in fluorescence mode, providing an energy resolution of 0.3 eV and edge energy precision better than 0.1 eV. After exposure to reaction conditions, the 0.5 wt.% and 1 wt.% Cu/CeO₂ samples were transferred into a glovebox under an inert atmosphere and loaded into sample holders. Data analysis, including coordination numbers (CNs) and bond distance calculations, was performed using WinXAS 3.1 software. Extended X-ray absorption fine structure (EXAFS) data were analyzed in *R*-space using standard fitting procedures. Cu–O and Cu–Cu coordination parameters were obtained using theoretical phase and amplitude files generated by full multiple scattering code for XAS (FEFF) calculations, with *So*² fixed at 0.85, calibrated using a Cu foil.

The surface copper atom concentration was determined through N₂O titration using a CATLAB unit (Hidden Analytical). In a typical experiment, 0.1 g of catalyst was placed in a fixed-bed reactor and reduced under H₂ (5 vol.%) / N₂ flow (30 mL·min⁻¹, heating rate 5 °C·min⁻¹) at 250 °C for 20 min. The integration of the N₂O concentration changes enabled calculation of the total amount of chemisorbed N₂O, assuming a stoichiometry of N₂O/Cu = 0.5. The mean Cu particle size (*d_p*) was estimated by assuming hemispherical particle geometry, using the equation: $d_p = 6M / (D\rho\sigma N_A)$, where *M* is the molecular weight of Cu (63.546 g·mol⁻¹), *D* is the fractional dispersion of Cu, ρ is the Cu metal density (8.94 g·cm⁻³), σ is the area occupied by a surface Cu atom (6.85 Å²·atom⁻¹), and *N_A* is Avogadro's constant.

XPS analysis was performed on a Kratos Axis Ultra DLD spectrometer with Al K α radiation (1486.6 eV). High-resolution spectra were acquired at a pass energy of 20 eV, while survey spectra were collected at 160 eV. A charge neutralizer minimized sample charging for improved spectral resolution, with the full width at half maximum (FWHM) of the fitted C 1s peak measuring approximately 1 eV. Binding energy values were referenced to the Fermi level, and the energy scale was calibrated using Au 4f_{7/2} at 84.0 eV and Cu 2p_{3/2} at 932.67 eV. Data analysis, including background subtraction and peak fitting with Gaussian/Lorentzian shapes, was carried out using CasaXPS software. Surface elemental concentrations were determined using Scofield factors and inelastic mean free path corrections. For *quasi in situ* measurements, samples were reduced in 5% H₂ for at least 2 h in a reaction cell connected to the spectrometer. Transfer between the reaction cell and the analysis chamber was conducted under ultrahigh vacuum to prevent air exposure. The oxidation state of copper was also evaluated using Cu LMM Auger electron spectroscopy. Spectra were collected with a PHI Versaprobe III system, and the Cu LMM kinetic energy was used to distinguish between Cu⁰ and Cu^I species.

This method, commonly referred to as the Rusche test, was used to differentiate metallic and oxidized copper based on characteristic peak positions. Electron paramagnetic resonance (EPR) measurements were performed on a Bruker EMXplus X-band spectrometer. Powdered samples were packed into quartz tubes and analyzed at room temperature. The technique was used to probe paramagnetic centers associated with oxygen vacancies in CeO₂.

In situ FTIR spectroscopy was conducted at the reaction temperature of 240 °C using a Bruker IFS-88 spectrometer to examine the intermediate species involved in the conversion of CO₂ to ethanol on the Cu/CeO_{2-x} catalyst. The spectrometer was operated in transmission-absorption mode with a resolution of 4 cm⁻¹. The experimental setup included a stainless-steel reaction cell fitted with CaF₂ windows and a resistance-heated furnace, with the catalyst positioned on a gold sample holder inside the cell.

2.3 Catalytic performance test and measurement of kinetics

Catalytic performance tests and kinetic measurements were carried out in a fixed-bed reactor. Prior to testing, the packed catalyst was activated at 400 °C for 2 h under a flow of H₂-He gas mixture (H₂/He = 1/9, 100 mL·min⁻¹). After activation, the reactor was purged with He at a flow rate of 50 mL·min⁻¹ for 15 min. Gas hourly space velocity (GHSV) values were adjusted by varying the catalyst packing amount and feed flow rates.

Quantitative product analysis was performed using an Agilent GC6890 gas chromatograph equipped with a flame ionization detector (FID) and a thermal conductivity detector (TCD). A Carboxen 1010 PLOT capillary column (30 m × 0.53 mm) was used for product separation. After an initial transient period, the catalyst typically exhibited stable performance over several hours. Unless otherwise specified, all reported data were collected at 10 min time-on-stream (TOS) during the steady-state period. Carbon mass balances were consistently within 96.2% ± 2.3%, and repeatability for quantitative analyses showed deviations of less than 1.3%. The absence of internal and external diffusion effects was verified using the Weisz-Prater criterion, while the Mears criterion was applied to confirm the absence of heat transfer limitations [19, 20].

2.4 DFT calculations

DFT calculations for the Cu/CeO₂ system were conducted using the Vienna *ab initio* simulation package (VASP) with the projector augmented wave method applied for ionic cores. The exchange-correlation interactions were treated with the PW91 functional in the generalized gradient approximation. The plane-wave energy cutoffs were set to 520 eV for bulk calculations and 400 eV for slab calculations [21, 22]. First-order Methfessel-Paxton smearing with a width of 0.15 eV was employed, with energies extrapolated to zero broadening. Self-consistent field calculations were performed with an energy convergence threshold of 10⁻⁵ eV, and structural relaxations proceeded until residual forces were less than 0.02 eV·Å⁻¹. To avoid interactions between periodic images, a vacuum layer exceeding 20 Å was included above the Cu/CeO₂ slab. For the surface Brillouin zone, p(2 × 2) unit cells were sampled using Monkhorst-Pack *k*-point grids with a 7 × 7 × 1 resolution. A Hubbard *U* correction of 5.0 eV was applied to the Ce 4f orbitals in all DFT + *U* calculations to account for strong on-site Coulomb interactions [23]. Both PW91 and Perdew-Burke-Ernzerhof (PBE) functionals were tested with *U*, yielding nearly identical energy

profiles (differences < 0.05 eV) for key steps in the reaction mechanism (see Table S5 in the Electronic Supplementary Material (ESM)). Therefore, DFT + *U* using PW91 was used throughout this study for consistency with the prior work.

Transition states (TS) were validated through vibrational normal mode analysis, confirming a single imaginary vibrational mode. Free energy corrections included zero-point energy (ZPE) adjustments, and entropy changes during adsorption were determined using the reaction temperature and a previously established relationship. The structures of TS in the reactions were identified using the dimer method and/or the climbing-image nudged elastic band (CI-NEB) method. Each transition state was verified through vibrational normal mode analysis, ensuring the presence of a single imaginary vibrational frequency. Multiple potential initial states were evaluated for calculating energy barriers, but only the pathway with the lowest energy barrier was considered in the analysis of reaction kinetics and selectivity.

3 Results and discussion

3.1 Results of catalyst structural characterization

Figure 1 presents the structural characterization of the 0.5% Cu/CeO₂ catalyst, demonstrating its morphology, elemental composition, and dispersion of copper over the ceria support. SEM images (Figs. 1(a) and 1(b)) reveal a porous and heterogeneous morphology, with rough and aggregated particles at a scale bar of 20 μm (Fig. 1(a)) and finer particle structures at 2 μm (Fig. 1(b)). TEM (Fig. 1(c)) confirms the well-resolved lattice fringes of ceria, indicating a well-defined crystalline structure. Energy dispersive X-ray spectroscopy (EDS) analysis (Fig. 1(d)) identifies prominent Ce, O, and Cu peaks, confirming the successful incorporation of 0.5 wt.% Cu. Powder XRD patterns (Fig. 1(e)) indicate a crystalline CeO₂ phase, with the absence of distinct Cu peaks suggesting high Cu dispersion or small particle sizes below the XRD detection limit. HAADF-STEM imaging (Fig. 1(f)) and EDS elemental mapping (Figs. 1(g)-1(i)) further confirm the uniform dispersion of Cu across the ceria support, with spatial correlations between Cu, O, and Ce. The overlay in Fig. 1(i), integrating HAADF-STEM and EDS Cu mapping, demonstrates intimate contact and homogeneous Cu dispersion on the ceria surface. The ICP-AES elemental analysis (Table S1 in the ESM) confirms that 0.25–2.0 wt.% Cu is successfully loaded onto CeO₂, and the spent Cu/CeO_{2-x} catalysts exhibit negligible Cu loss, indicating their stability under reaction conditions. BET measurements (Table S2 in the ESM) indicate that the surface areas of the Cu/CeO_{2-x} catalysts range from 45 to 52 m²·g⁻¹, with pore sizes between 1.9 and 2.5 nm and pore volumes in the range of 0.25 to 0.32 cm³·g⁻¹.

3.2 Results of catalytic performance for CO₂ hydrogenation to ethanol

While GHSV is varied at 30–120 mL·g_{cat}⁻¹·h⁻¹, Fig. 2 presents the catalytic performance of the 0.5% Cu/CeO_{2-x} catalyst for CO₂ hydrogenation to ethanol under reaction conditions of 2.5 g catalyst, 30 atm, H₂/CO₂ = 3, and 240 °C. The results highlight key aspects of ethanol selectivity, CO₂ conversion, reaction kinetics, temperature effects, and catalyst stability. The ethanol selectivity versus CO₂ conversion plot (Fig. 2(a)) shows an inverse relationship, where high ethanol selectivity (~ 100%) is achieved at low CO₂ conversion (< 10%), indicating the suppression of

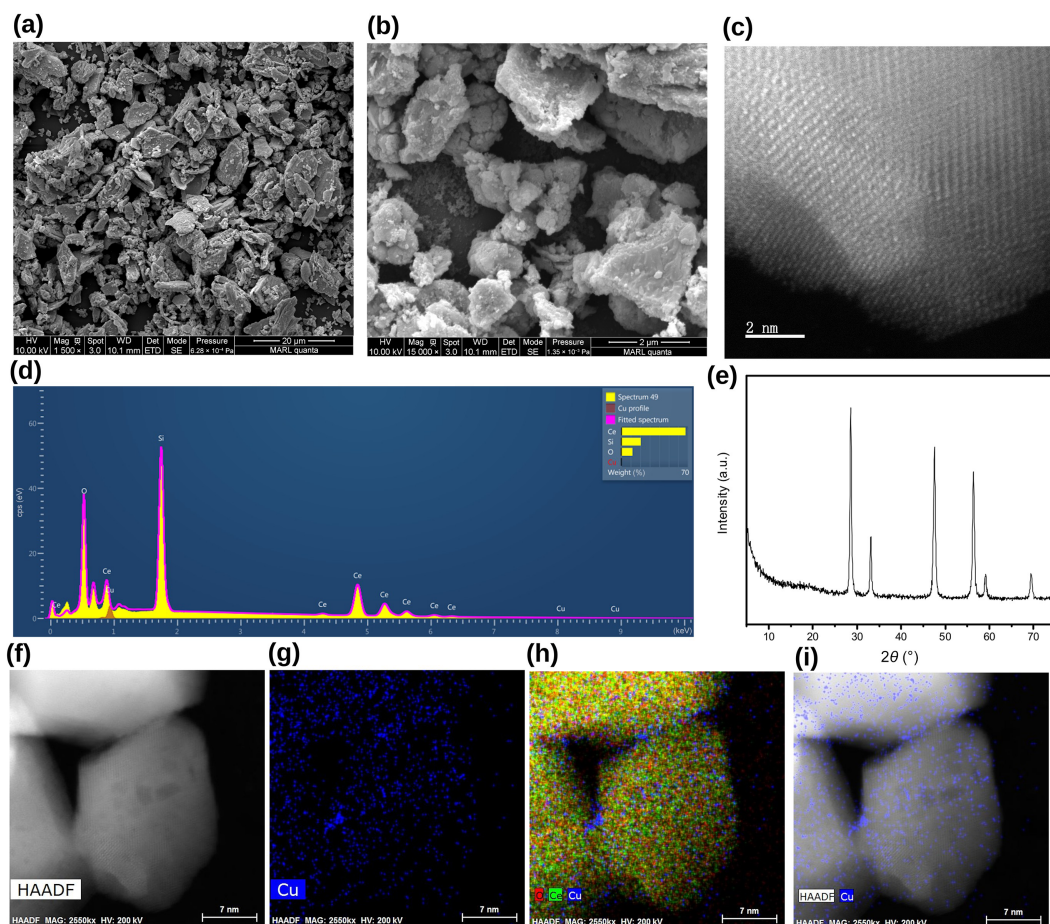


Figure 1 Structural characterization of the 0.5% Cu/CeO₂ catalyst: ((a) and (b)) SEM images at scale bars of 20 and 5 μm, showing surface morphology; (c) TEM image at a scale bar of 2 nm, revealing lattice fringes; (d) EDS spectrum, confirming elemental composition; (e) powder XRD pattern, indicating the crystalline structure; (f) HAADF-STEM image, illustrating contrast differences; (g) EDS elemental mapping for Cu, showing its distribution; (h) EDS elemental mapping for O, Ce, and Cu, highlighting element dispersion; and (i) HAADF-STEM image overlaid with EDS Cu mapping, confirming Cu dispersion on the CeO₂ support.

undesired side reactions. However, as CO₂ conversion increases, ethanol selectivity declines, suggesting that secondary reactions, such as CH₄, CO formation, and trace CH₃OH, become more pronounced. The suppression of CH₄ and CO formation is attributed to the combination of low reaction temperature and the small size of Cu particles [24], while the suppression of CH₃OH is enabled by the synergistic interaction between Cu^I sites and oxygen vacancies, which promotes C–C coupling toward ethanol. This trend underscores the trade-off between maximizing CO₂ conversion and maintaining high ethanol selectivity, which is a critical factor in optimizing catalytic performance for industrial applications. The ethanol production rate is strongly influenced by Cu particle size, as shown in Fig. 2(b), where smaller Cu particles (≤ 4 nm) exhibit significantly higher ethanol production rates. This observation highlights the importance of controlling Cu particle size during catalyst synthesis to enhance catalytic activity. The observed decrease in ethanol formation with increasing Cu particle size is attributed to the reduced surface area of active Cu sites and potential changes in electronic properties. The effect of reaction temperature on CO₂ conversion and product distribution is depicted in Fig. 2(c), showing that CO₂ conversion increases with temperature, reaching a peak due to enhanced reaction kinetics at higher temperatures. However, ethanol selectivity declines as temperature increases, accompanied by a rise in undesired products, such as CH₄ and CO. Notably, minimal coke formation is

observed across all temperatures, indicating that the catalyst retains structural integrity and resists deactivation. These results emphasize that while higher temperatures improve CO₂ conversion, they compromise ethanol selectivity, necessitating a careful balance in operating conditions. The long-term stability of the 0.5% Cu/CeO_{2-x} catalyst was evaluated over 72 h of continuous operation (Fig. 2(d)). The CO₂ conversion (~ 5%) and ethanol selectivity (~ 95%) remain remarkably stable, with no significant signs of deactivation or performance decline. Extended catalyst stability testing from 72 to 144 h demonstrated sustained performance without loss in CO₂ conversion or ethanol selectivity (Fig. S1 in the ESM). Post-reaction characterizations, including SEM (Fig. S2 in the ESM) and XRD (Fig. S3 in the ESM), confirmed the preservation of the fluorite CeO₂ structure and the morphological stability of the catalyst, indicating no significant sintering or structural degradation after prolonged operation.

This sustained high selectivity and stability demonstrate the robustness of the catalyst, confirming its potential for practical applications in CO₂ utilization and sustainable ethanol production. The data is among the promising performances of converting CO₂ to ethanol. Recent studies have reported varying efficiencies in CO₂ hydrogenation to ethanol. For instance, a Cu(I)-Hong Kong University of Science and Technology (HKUST)-17.5 catalyst achieved a CO₂ conversion of 41.2% with 62.9% ethanol selectivity under ambient conditions [25]. Another study utilizing a Ru-based

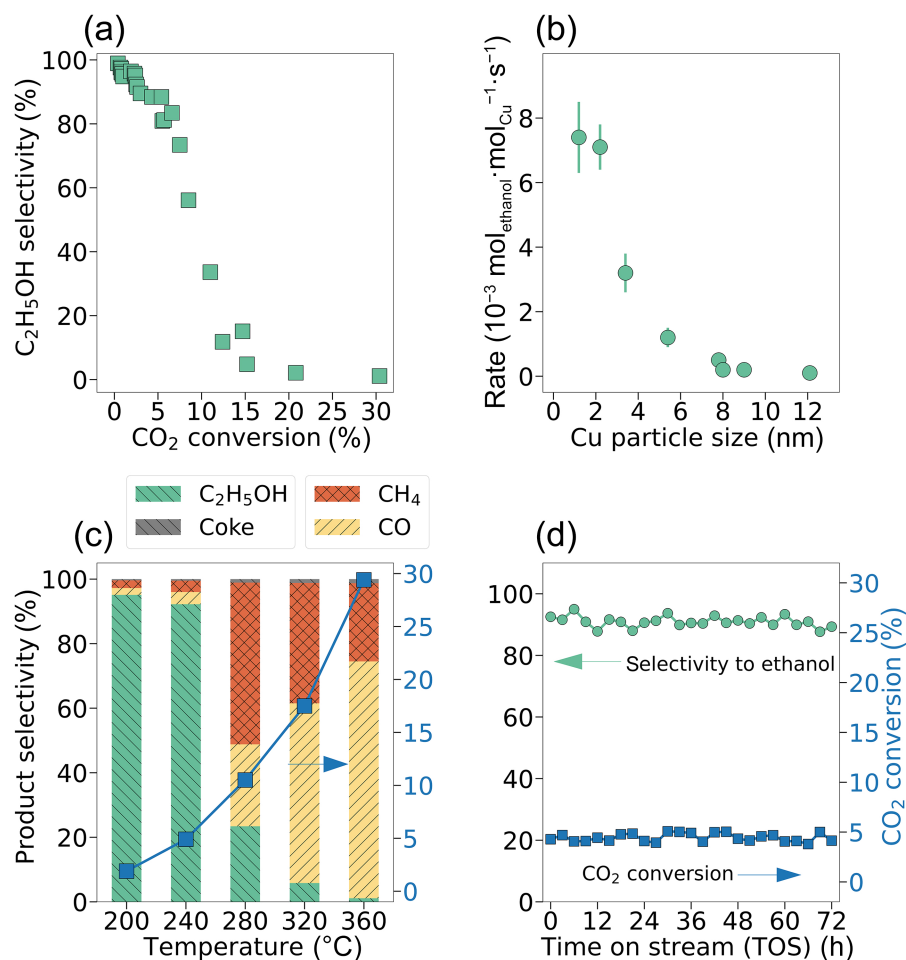


Figure 2 Catalytic performance of the 0.5% Cu/CeO_{2-x} catalyst for CO₂ hydrogenative coupling to ethanol: (a) ethanol selectivity vs. CO₂ conversion by varying GHSV, showing the trade-off between conversion and selectivity; (b) ethanol production rate vs. Cu particle size, highlighting the impact of particle size on catalytic efficiency; (c) effect of reaction temperature on CO₂ conversion and product distribution, illustrating selectivity trends with temperature variation; and (d) catalyst stability over a 72-h TOS, demonstrating long-term performance. Standard reaction conditions: 2.5 g 0.5% Cu/CeO₂ catalyst, 30 atm, H₂/CO₂ = 3, 240 °C, GHSV = 120 mL·g_{cat}⁻¹·h⁻¹.

catalyst reported approximately 70% ethanol selectivity, with CO as the primary byproduct [26]. Additionally, Pd₂Cu nanoparticles supported on P25 exhibited an ethanol selectivity of up to 92.5% and a turnover frequency of 359 h⁻¹ [27]. While the conversion rate is lower, the significantly higher selectivity underscores the catalyst's potential for producing high-purity ethanol, minimizing byproduct formation.

3.3 Discussion of potential active sites for CO₂ hydrogenative coupling to ethanol

Figure 3 presents the experimental investigations into the active sites responsible for CO₂ hydrogenative coupling to ethanol over Cu/CeO_{2-x} catalysts. The *quasi in situ* XPS of Ce 3d (Fig. 3(a)) reveals the distribution of Ce^{III} and Ce^{IV} oxidation states at different Cu loadings (0.25–2.0 wt.%). An increase in Ce^{III} content with higher Cu loading is observed, with the Ce^{III} fraction rising from 27% at 0.25% Cu loading to 37% at 2.0% Cu loading, suggesting that Cu incorporation promotes CeO₂ reduction to CeO_{2-x} and enhances O_v formation. This is further supported by the O 1s XPS spectra (Fig. 3(b)), which deconvolute into three distinct oxygen species: lattice oxygen (O_{lat}), adsorbed oxygen (O_{ad}), and O_v. The proportion of O_v increases significantly with Cu loading, reaching 54% at 2.0% Cu, demonstrating that oxygen vacancies play a critical

role in CO₂ activation and hydrogenation. Notably, the Cu^I content is consistent with the *in situ* X-ray absorption near-edge structure (XANES) measurements and fitting results (Table S3 in the ESM).

The Cu 2p XPS spectra (Fig. 3(c)) indicate the presence of Cu⁰, Cu^I, and Cu^{II} species. As Cu loading decreases, Cu^{II} species dominate, while higher Cu loadings result in increased Cu⁰ species, likely due to weaker metal-support interactions in larger Cu particles. EPR analysis of the reduced catalyst reveals a distinct signal at $g \approx 2.003$ (Fig. S4 in the ESM), indicative of paramagnetic F-centers associated with oxygen vacancies in CeO_{2-x}. This result confirms that reduction treatment generates oxygen vacancies, which are proposed to cooperate with Cu^I sites in promoting selective CO₂ hydrogenative coupling. Although Cu⁰ and Cu^I exhibit nearly identical Cu 2p_{3/2} binding energies (~932.6 eV), Cu LMM Auger analysis (Fig. S5 in the ESM) provides further distinction based on kinetic energy. The LMM spectrum shows a dominant signal at ~916.7 eV (Cu^I), confirming that the majority species is Cu^I. The consistency between the Cu^I content estimated by XPS (58%) and LMM (54%) supports the reliability of the deconvolution. Notably, Cu^I species, which are considered catalytically active for CO₂ hydrogenation, are more prevalent at lower Cu loadings (Cu^I = 69% at 0.25% Cu vs. Cu^I = 31% at 2.0% Cu). These observations suggest that both Cu^I and O_v species play

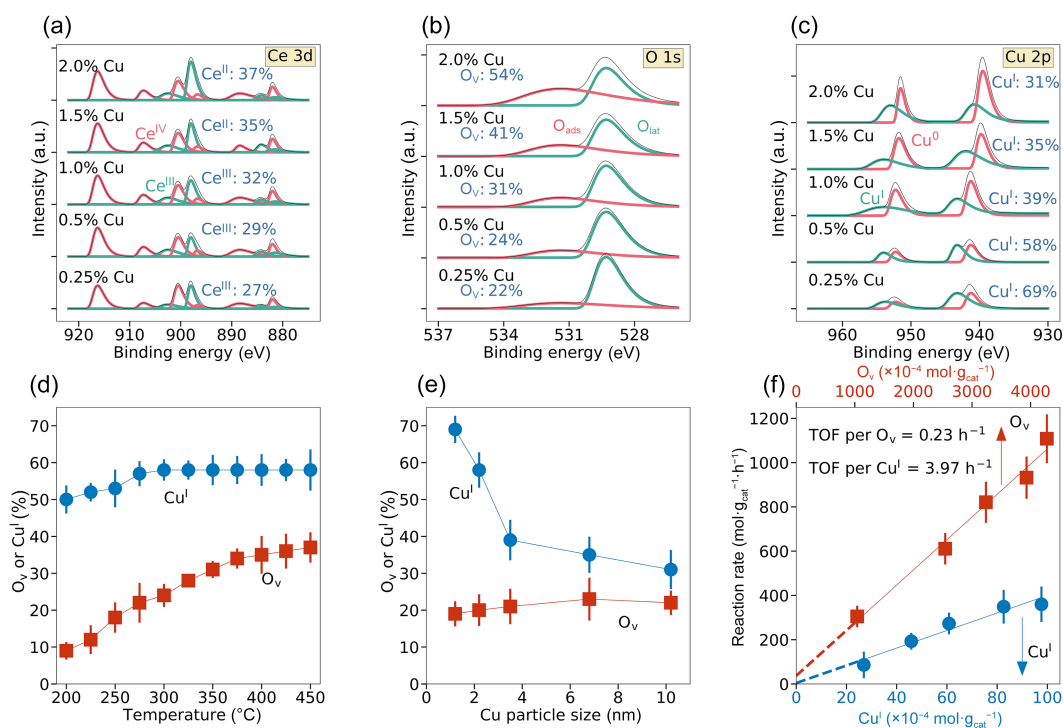


Figure 3 Experimental investigations of active sites in Cu/CeO₂ catalysts for CO₂ hydrogenative coupling to ethanol: (a) XPS spectra of Ce 3d, showing the distribution of Ce^{III} and Ce^{IV} oxidation states; (b) XPS spectra of O 1s, revealing the presence of O_{lat}, O_{ads}, and O_v; (c) XPS spectra of Cu 2p, indicating the relative proportions of Cu^I, Cu^{II}, and Cu⁰ species; (d) dependence of O_v concentration on reduction temperature, illustrating its tunability; (e) dependence of Cu^I concentration on Cu loading, highlighting its variation with particle size; and (f) site-specific reaction rate analysis, showing a linear correlation between catalytic activity and the combined presence of Cu^I and O_v, confirming their synergistic role in ethanol formation.

key roles in CO₂ hydrogenative coupling to ethanol formation. However, their concentrations exhibit opposite trends with Cu loading, raising the question: Is O_v alone, Cu^I alone, or both Cu^I and O_v responsible for CO₂ hydrogenation to ethanol? To address this question, we independently varied either O_v or Cu^I and examined their effects on catalytic activity. To decouple the roles of Cu^I and oxygen vacancies, Cu loading and reduction temperature were independently varied. O_v concentration was modulated by thermal reduction (200–450 °C) of a constant 0.5 wt.% Cu/CeO_{2-x} catalyst (Fig. 3(d)), while Cu^I content was tuned by adjusting Cu loading under controlled reduction temperatures at 300–400 °C (Fig. 3(e)). The nearly constant Cu particle size (~ 2 nm) across reduction temperatures and its correlation with Cu^I suggest that particle size is not the primary variable influencing CO₂ conversion. Instead, the synergistic effect between Cu^I and O_v is proposed to govern the catalytic behavior. Figure 3(d) shows that O_v increases with reduction temperature (300–450 °C), while Cu^I remains nearly constant, allowing us to investigate the impact of O_v variations on catalytic activity. Conversely, to independently vary Cu^I, catalysts with different Cu loadings (and thus different Cu particle sizes) were subjected to reduction at specific temperatures chosen to maintain a constant O_v concentration (~ 20%), as shown in Fig. 3(e). This approach enabled us to study the dependence of reaction rates on O_v and Cu^I separately. The CNs of Cu–Cu in 0.5% Cu/CeO_{2-x} and 1.0% Cu/CeO_{2-x} are 1.8 and 3.5, respectively (Table S4 in the ESM), while the CNs of Cu–O are 2.0 and 1.7. These low CN values indicate a strong interaction between Cu particles and the CeO₂ support, suggesting significant synergy of Cu and CeO₂.

The catalytic TOFs, determined from these experiments (Fig. 3(f)), show a linear correlation between reaction rates and both

O_v and Cu^I contents. The calculated TOFs are 0.23 h⁻¹ per O_v site and 3.97 h⁻¹ per Cu^I site, with both correlations passing through the origin. This finding strongly indicates that neither Cu^I nor O_v alone can serve as the active site—rather, their synergy is essential for CO₂ hydrogenation to ethanol. As shown in Fig. 3(f), the reaction rate approaches zero when either Cu^I or O_v is absent, confirming their cooperative role. Cu^I facilitates CO₂ activation, while O_v stabilizes key intermediates and promotes C–C coupling, both of which are crucial for selective ethanol synthesis. The interplay between Cu^I and O_v not only enhances CO₂ activation but also ensures the efficient coupling of two C₁ species to form ethanol, providing key insights into the active site requirements for selective CO₂ hydrogenation.

3.4 Discussion of potential reaction pathway for CO₂ hydrogenation to ethanol

The mechanism of C–C bond formation in CO₂ hydrogenative coupling to ethanol remains a subject of debate in the literature. Various coupling pathways have been proposed, with key intermediates, such as CH₃, CH₂, CH₂OH, and CO [28–30]. To clarify the reaction mechanism, we employed *operando* FTIR spectroscopy to track the surface-bound intermediates under reaction conditions and performed DFT calculations to analyze the energetics of the proposed pathways over Cu/CeO₂ catalysts.

Operando FTIR spectroscopy reveals multiple C₁ surface species involved in CO₂ hydrogenation, including CH₂OH, CH₂, CO*, COO*, and HCOO*. The presence of CO₂^{δ-} species, characterized by vibrational peaks at ~ 1600 and 1280 cm⁻¹, confirms initial CO₂ activation, leading to hydrogenation. However, COO* (~ 1603 cm⁻¹) and HCOO* (1590 and 1370 cm⁻¹) remain over-

oxidized to facilitate C–C bond formation. A distinct 1025 cm^{-1} peak confirms the formation of CH_2OH^* , a key intermediate in the formate-mediated pathway. Further hydrogenation leads to CH_2^* , identified by a peak at $\sim 1220\text{ cm}^{-1}$, representing a more reduced and reactive species. The simultaneous detection of CH_2OH and CH_2^* supports their critical role in ethanol formation. Therefore, we propose that CH_2OH and CH_2^* are the primary intermediates in C–C coupling, while CO , COO , and HCOO^* remain insufficiently reduced to participate directly in this step.

To evaluate the synergistic effect between Cu and oxygen vacancies, three different vacancy sites are investigated using DFT calculations: a bulk-like vacancy within CeO_2 , a surface vacancy away from Cu, and an interfacial vacancy directly adjacent to Cu at the Cu/ CeO_2 interface (see Fig. S6 in the ESM). Among those possible sites, the interfacial vacancy exhibited the lowest formation energy, indicating it is the most stable configuration. This model was used in all subsequent calculations to reflect the synergistic interaction between Cu and O_v at the interface. Comparisons between DFT and DFT + U show that the inclusion of U improves the accuracy of Ce 4f state localization and modifies the intermediate binding energies (Fig. S7 in the ESM).

DFT calculations further validate the reaction coordinate for CH_2OH and CH_2 coupling, as shown in Fig. 4. The calculated free energy profiles at $240\text{ }^\circ\text{C}$ illustrate the stepwise formation of CH_2OH^* , CH_2^* , and their coupling to ethanol. The formation of H_2CO (Fig. 4(a)) follows sequential hydrogenation of CO_2 with two H_2 molecules, progressing through COO and H_2COOH

intermediates. The highest energy barriers, TS2 ($\sim 1.1\text{ eV}$) and TS3 ($\sim 1.3\text{ eV}$), correspond to the conversion of COO to H_2COOH and its subsequent hydrogenation, confirming these steps as kinetically limiting. Similarly, CH_2 formation (Fig. 4(b)) proceeds through stepwise CO_2 hydrogenation via OCO^* , COH^* , C^* , and CH^* intermediates, with TS6 ($\sim 1.2\text{ eV}$) and TS8 ($\sim 1.4\text{ eV}$) representing the most challenging transformations. The final and most crucial step (Fig. 4(c)), C–C coupling between H_2CO^* and CH_2^* , proceeds through TS11, TS12, and TS13, with TS12 ($\sim 1.0\text{ eV}$) being the highest barrier, indicating that this step is feasible under reaction conditions but remains a key determinant of ethanol selectivity. The strong agreement between *operando* FTIR observations and DFT calculations establishes CH_2OH^* and CH_2^* as the dominant C–C coupling intermediates in CO_2 hydrogenative ethanol synthesis. These findings provide new mechanistic insights into selective ethanol formation from CO_2 , further supporting the essential role of Cu^I and O_v active sites in facilitating CO_2 activation, hydrogenation, and C–C coupling.

4 Conclusions

This study provides a comprehensive investigation into the structural, catalytic, and mechanistic aspects of CO_2 hydrogenative coupling to ethanol over Cu/ CeO_{2-x} catalysts. Structural characterization confirms the high dispersion of Cu and its strong interaction with CeO_2 , contributing to catalyst stability and activity. Catalytic performance analysis demonstrates that ethanol selectivity

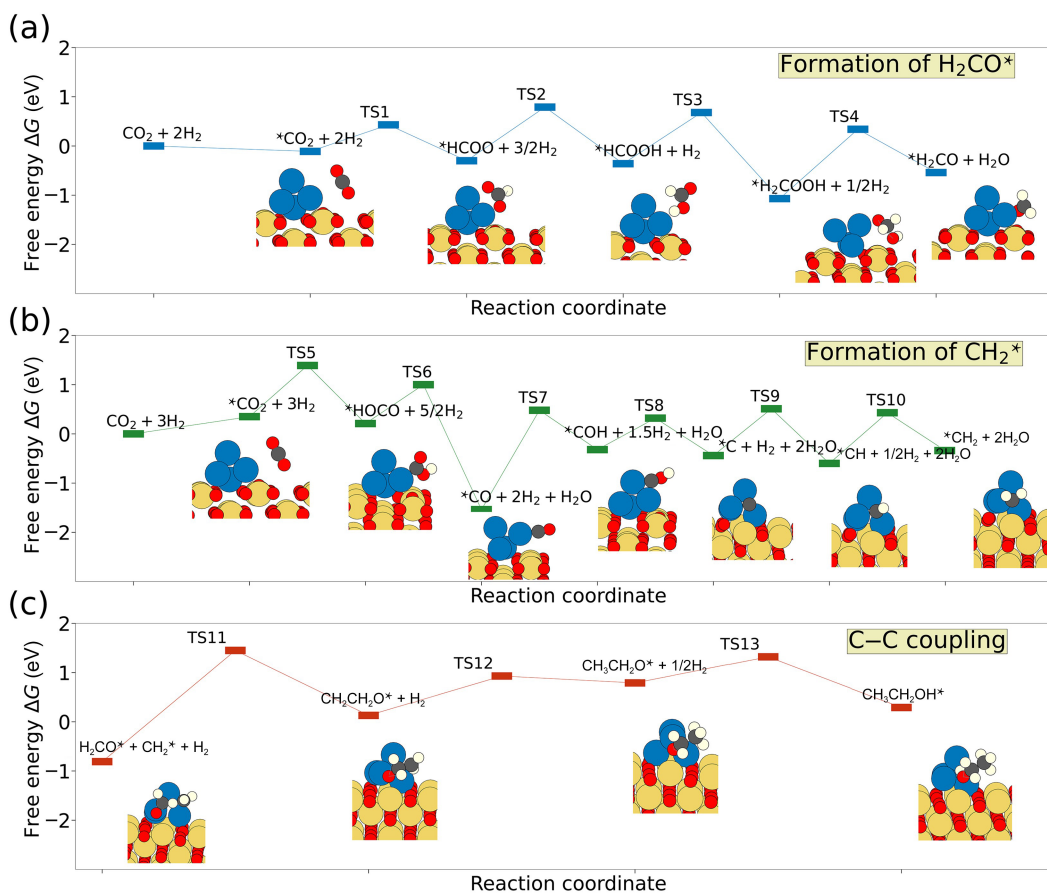


Figure 4 DFT calculations on the hydrogenative coupling of CO_2 to ethanol over Cu/ CeO_2 catalysts: (a) reaction pathway for the formation of H_2CO^* , showing the sequential hydrogenation of CO_2 -derived intermediates; (b) reaction pathway for the formation of CH_2^* , illustrating stepwise hydrogenation through COH^* , C^* , and CH^* intermediates; and (c) pathway for C–C coupling between H_2CO^* and CH_2^* , demonstrating the key steps leading to ethanol formation.

(~ 95%) is maximized at low CO₂ conversion (~ 5%), and that small Cu particles (≤ 4 nm) exhibit superior ethanol production rates, emphasizing the role of Cu particle size in tuning catalytic behavior. Through *quasi in situ* XPS and independent control of Cu^I and O_v concentrations, we established that neither Cu^I nor O_v alone serves as the active site; rather, their synergistic interaction is essential for CO₂ activation and ethanol formation, with TOFs of 0.23 h⁻¹ per O_v site and 3.97 h⁻¹ per Cu^I site. *Operando* FTIR spectroscopy and DFT calculations further reveal that CH₂OH and CH₂ are the primary intermediates responsible for C–C bond formation, while CO*, COO*, and HCOO* remain too oxidized to participate in coupling. The reaction coordinate analysis identifies TS12 (~ 1.0 eV) as the rate-limiting step, underscoring the importance of C–C bond formation in determining ethanol selectivity. These findings provide fundamental insights into the active site requirements and reaction pathways for CO₂ hydrogenative coupling to ethanol. A deep understanding of these mechanisms is crucial for advancing CO₂ conversion technologies, enabling sustainable ethanol production, and contributing to CO₂ emissions reduction. The mechanistic insights gained in this study offer valuable guidance for rational catalyst design, ultimately improving the efficiency and selectivity of CO₂ hydrogenation to ethanol.

Electronic Supplementary Material: Supplementary material (including Table S1 (ICP-AES elemental analysis), Table S2 (BET surface area, pore size, and pore volume), Table S3 (XANES fitting results), and Table S4 (*k*²-weighted EXAFS fitting results) for Cu/CeO_{2-x} catalysts reduced at 400 °C. These data provide additional insights into the catalysts' composition, textural properties, and electronic structure. Table S5 presents a comparison of PW91 and PBE functionals. Figure S1 shows additional catalyst stability testing from 72 to 144 h TOS, demonstrating long-term performance under standard reaction conditions (2.5 g 0.5% Cu/CeO₂). Figure S2 provides a SEM image (20 μm scale) of the spent 0.5 wt.% Cu/CeO₂ catalyst. Figure S3 shows the powder XRD pattern of the spent 0.5 wt.% Cu/CeO_{2-x} catalyst. Figure S4 presents the EPR spectrum of the 0.5 wt.% Cu/CeO_{2-x} catalyst. Figure S5 displays the Cu LMM Auger spectrum of the spent 0.5 wt.% Cu/CeO_{2-x} catalyst. Figure S6 illustrates the DFT model for the synergistic interaction between Cu and O_v. Figure S7 compares DFT + *U* (filled bars) and standard DFT (unfilled bars) calculations for the hydrogenative coupling of CO₂ to ethanol over Cu/CeO₂, highlighting the effect of Hubbard *U* correction (*U* = 5.0 eV) on the adsorption and reaction energies of key intermediates) is available in the online version of this article at <https://doi.org/10.26599/NR.2025.94907518>.

Data availability

All data needed to support the conclusions in the paper are presented in the manuscript and the Electronic Supplementary Material. Additional data related to this paper may be requested from the corresponding author upon request.

Acknowledgements

Y. X., J. H., and J. P. W. acknowledge financial support from the College of Engineering and Science (COES)'s Startup Fund at Louisiana Tech University, the TIRE Grant from the Louisiana Transportation Research Center (LTRC), and the Research

Enhancement Awards (REA) from the Louisiana Space Consortium (LaSPACE). This work is supported in part by the U.S. National Science Foundation under grant (No. OIA-1946231) and the Louisiana Board of Regents for the Louisiana Materials Design Alliance (LAMDA). Y. W., P. L. H., F. Y. acknowledge financial support from Y. W.'s Herbert L. Stiles Professorship.

Declaration of competing interest

All the contributing authors report no conflict of interests in this work.

Author contribution statement

Y. X. and Y. W. conceived the idea and supervised the project. J. H., P. L. H., and F. Y. designed and performed the experiments. J. P. W. carried out DFT calculations under the supervision of Y. X. and D. S. M. N. J. L. and J. T. M. conducted the spectroscopic characterizations. All authors contributed to the discussion of the results and writing of the manuscript. All the authors have approved the final manuscript.

Use of AI statement

None.

References

- Ye, R.; Ding, J.; Reina, T. R.; Duyar, M. S.; Li, H.; Luo, W.; Zhang, R.; Fan, M.; Feng, G.; Sun, J. et al. Design of catalysts for selective CO₂ hydrogenation. *Nat. Synth.* **2025**, *4*, 288–302.
- Du, P.; Ait El Fakir, A.; Zhao, S.; Dostagir, N. H. M. D.; Pan, H.; Ting, K. W.; Mine, S.; Qian, Y.; Shimizu, K.; Toyao, T. Ethanol synthesis via catalytic CO₂ hydrogenation over multi-elemental KFeCuZn/ZrO₂ catalyst. *Chem. Sci.* **2024**, *15*, 15925–15934.
- Zeng, F.; Mebrahtu, C.; Xi, X.; Liao, L.; Ren, J.; Xie, J.; Heeres, H. J.; Palkovits, R. Catalysts design for higher alcohols synthesis by CO₂ hydrogenation: Trends and future perspectives. *Appl. Catal. B: Environ.* **2021**, *291*, 120073.
- Latsiou, A. I.; Charisiou, N. D.; Frontistis, Z.; Bansode, A.; Goula, M. A. CO₂ hydrogenation for the production of higher alcohols: Trends in catalyst developments, challenges and opportunities. *Catal. Today* **2023**, *420*, 114179.
- Yang, Y. X.; White, M. G.; Liu, P. Theoretical study of methanol synthesis from CO₂ hydrogenation on metal-doped Cu (111) surfaces. *J. Phys. Chem. C* **2012**, *116*, 248–256.
- Liu, L. N.; Fan, F.; Jiang, Z.; Gao, X. F.; Wei, J. J.; Fang, T. Mechanistic study of Pd–Cu bimetallic catalysts for methanol synthesis from CO₂ hydrogenation. *J. Phys. Chem. C* **2017**, *121*, 26287–26299.
- Liu, L. N.; Fan, F.; Bai, M. M.; Xue, F.; Ma, X. R.; Jiang, Z.; Fang, T. Mechanistic study of methanol synthesis from CO₂ hydrogenation on Rh-doped Cu (111) surfaces. *Mol. Catal.* **2019**, *466*, 26–36.
- Murthy, P. S.; Wang, Z.; Wang, L.; Zhao, J.; Wang, Z.; Liang, W.; Huang, J. Improved CO₂ hydrogenation on Ni–ZnO/MCM-41 catalysts with cooperative Ni and ZnO sites. *Energy & Fuels* **2020**, *34*, 16320–16329.
- Liu, L. N.; Yao, H. D.; Jiang, Z.; Fang, T. Theoretical study of methanol synthesis from CO₂ hydrogenation on PdCu₃ (111) surface. *Appl. Surf. Sci.* **2018**, *451*, 333–345.
- Behrens, M.; Studt, F.; Kasatkina, I.; Kühl, S.; Hävecker, M.; Abild-Pedersen, F.; Zander, S.; Girgsdies, F.; Kurr, P.; Knief, B. L. et al. The active site of methanol synthesis over Cu/ZnO/Al₂O₃ industrial catalysts. *Science* **2012**, *336*, 893–897.

- [11] Kattel, S.; Ramirez, P. J.; Chen, J. G.; Rodriguez, J. A.; Liu, P. Active sites for CO₂ hydrogenation to methanol on Cu/ZnO catalysts. *Science* **2017**, *355*, 1296–1299.
- [12] Kondratenko, E. V.; Mul, G.; Baltrusaitis, J.; Larrazabal, G. O.; Pérez-Ramírez, J. Status and perspectives of CO₂ conversion into fuels and chemicals by catalytic, photocatalytic, and electrocatalytic processes. *Energy Environ. Sci.* **2013**, *6*, 3112–3135.
- [13] Wang, W.; Jiang, X.; Wang, X.; Song, C. Fe–Cu bimetallic catalysts for selective CO₂ hydrogenation to olefin-rich C₂⁺ hydrocarbons. *Ind. Eng. Chem. Res.* **2018**, *57*, 4535–4542.
- [14] Zhang, Q. H.; Kang, J. C.; Wang, Y. Development of novel catalysts for Fischer–Tropsch synthesis: Tuning the product selectivity. *ChemCatChem* **2010**, *2*, 1030–1058.
- [15] Li, Z.; Wu, W.; Wang, M.; Wang, Y.; Ma, X.; Luo, L.; Chen, Y.; Fan, K.; Pan, Y.; Li, H. et al. Ambient-pressure hydrogenation of CO₂ into long-chain olefins. *Nat. Commun.* **2022**, *13*, 2396.
- [16] Vogt, C.; Monai, M.; Sterk, E. B.; Palle, J.; Melcherts, A. E. M.; Zijlstra, B.; Groeneveld, E.; Berben, P. H.; Boereboom, J. M.; Hensen, E. J. M. et al. Understanding carbon dioxide activation and carbon–carbon coupling over nickel. *Nat. Commun.* **2019**, *10*, 5330.
- [17] Cheng, K.; Li, Y.; Kang, J.; Zhang, Q.; Wang, Y. Selectivity control by relay catalysis in CO and CO₂ hydrogenation to multicarbon compounds. *Acc. Chem. Res.* **2024**, *57*, 714–725.
- [18] Nie, X.; Wang, H.; Janik, M. J.; Chen, Y.; Guo, X.; Song, C. Mechanistic insight into C–C coupling over Fe–Cu bimetallic catalysts in CO₂ hydrogenation. *J. Phys. Chem. C* **2017**, *121*, 13164–13174.
- [19] Weisz, P. B.; Prater, C. D. Interpretation of measurements in experimental catalysis. *Adv. Catal.* **1954**, *6*, 143–196.
- [20] Mears, D. E. Diagnostic criteria for heat transport limitations in fixed bed reactors. *J. Catal.* **1971**, *20*, 127–131.
- [21] Kresse, G.; Furthmüller, J. Efficient iterative schemes for *ab initio* total-energy calculations using a plane-wave basis set. *Phys. Rev. B* **1996**, *54*, 11169–11186.
- [22] Campbell, C. T.; Árnadóttir, L.; Sellers, J. R. V. Kinetic prefactors of reactions on solid surfaces. *Z. Phys. Chem.* **2013**, *227*, 1435–1454.
- [23] Plata, J. J.; Márquez, A. M.; Fdez. Sanz, J. Communication: Improving the density functional theory + *U* description of CeO₂ by including the contribution of the O 2p electrons. *J. Chem. Phys.* **2012**, *136*, 041101.
- [24] Reske, R.; Mistry, H.; Behafarid, F.; Roldan Cuenya, B.; Strasser, P. Particle size effects in the catalytic electroreduction of CO₂ on Cu nanoparticles. *J. Am. Chem. Soc.* **2014**, *136*, 6978–6986.
- [25] Zou, N.; Chen, J.; Qiu, T.; Zheng, Y. Direct hydrogenation of CO₂ to ethanol at ambient conditions using Cu(I)-MOF in a dielectric barrier discharge plasma reactor. *J. Mater. Chem. A* **2023**, *11*, 10766–10775.
- [26] Zhou, C. S.; Aitbekova, A.; Liccardo, G.; Oh, J.; Stone, M. L.; McShane, E. J.; Werghi, B.; Nathan, S.; Song, C. Y.; Ciston, J. et al. Steam-assisted selective CO₂ hydrogenation to ethanol over Ru–In catalysts. *Angew. Chem., Int. Ed.* **2024**, *63*, e202406761.
- [27] Tan, A. F. J.; Isnaini, M. D.; Phisalaphongb, M.; Yip, A. C. K. The engineering of CO₂ hydrogenation catalysts for higher alcohol synthesis. *RSC Sustain.* **2024**, *2*, 3638–3654.
- [28] Asare Bediako, B. B.; Qian, Q.; Han, B. Synthesis of C₂₊ chemicals from CO₂ and H₂ via C–C bond formation. *Acc. Chem. Res.* **2021**, *54*, 2467–2476.
- [29] Xu, D.; Wang, Y.; Ding, M.; Hong, X.; Liu, G.; Tsang, S. C. E. Advances in higher alcohol synthesis from CO₂ hydrogenation. *Chem* **2021**, *7*, 849–881.
- [30] Kattel, S.; Liu, P.; Chen, J. G. Tuning selectivity of CO₂ hydrogenation reactions at the metal/oxide interface. *J. Am. Chem. Soc.* **2017**, *139*, 9739–9754.



This is an open access article under the terms of the Creative Commons Attribution 4.0 International License (CC BY 4.0, <https://creativecommons.org/licenses/by/4.0/>).

© The Author(s) 2025. Published by Tsinghua University Press.